Experimental Investigation of a Turbulent Transpiration-induced Channel Flow Using Particle Image Velocimetry Technique*

By

Zhiqun Deng (1) , Ronald J. Adrian (2)

Laboratory for Turbulence and Complex Flow
Dept. of Theoretical and Applied Mechanics
University of Illinois, Urbana, Illinois 61801

(1) E-mail: deng1@uiuc.edu
(2) E-mail: r-adrian@uiuc.edu

Abstract

Turbulence in a channel flow with a fully transpired wall has been investigated experimentally. 2D Particle Image Velocimetry is used to measure the instantaneous flow fields within the channel for two different porous surfaces: 6.35 mm honeycomb and 3.175 mm honeycomb. In this paper, the 6.35 mm honeycomb creates a larger fluctuation of the injection velocity than the 3.175 mm honeycomb does (a factor of 1.7). Mean flow properties and statistics are obtained by analyzing the instantaneous measurements. Comparisons with analytical and computational results are made. It is found that the boundary conditions on the porous surface are very important to the internal core flow evolution and flow pattern. For a coarse porous surface (in this paper, the 6.35 mm honeycomb with higher perturbation level on the transpiration surface), the mean flow differs significantly from the classical laminar solution and computational results, and much more turbulent shear stress is indicated. However, with small pore size (in this paper, the 3.175 mm honeycomb with relatively lower perturbation level on the surface), the mean velocity profiles are very close to the analytical laminar solution for a considerable downstream length, and the turbulent shear stress is much smaller than in the first case. Therefore, profound modification of the flow structure can occur due to the effect of non-ideal wall boundary conditions on the porous surface. In addition, the location where the maximum RMS and turbulent shear stress velocity occurs moves closer to the porous surface with increasing downstream position.[1]

* This work is supported by the U.S. Department of Energy through CSAR at UIUC.

Introduction

Transpiration-induced channel flow is an unusual form of wall turbulence because the turbulence is created by the release of fluid normal to the wall, as opposed to friction associated with flow parallel to the wall. Consequently, conventional turbulence modeling is suspect. This paper describes experiments conducted to provide insight into the essential features of such flows for the purpose of supporting the development and validation of numerical computations based on RANS and large eddy simulation. This study uses a cold, incompressible flow produced by a single transpired wall in a rectangular cavity (Figure 1), which has turbulence production similar to the more complicated reacting flow. It is found that the details of the wall boundary condition, in the form of the amplitude and scale of the flow perturbations at the wall, have a profound effect on the turbulent flow in the core. Two different transpiration surfaces are used to investigate this effect. Measurements of the instantaneous velocity field using 2D Particle Image Velocimetry (PIV) indicate flow behavior ranging from negligible turbulence effect with a nearly laminar velocity profile to a strongly effected flow with a blunt mean velocity profile, depending on the surface and perturbation scale.

Taylor [1] and Culick [2] deduced the inviscid, laminar, self-similar solution to the problem of core flow within a cylindrical chamber with uniform wall injection. The analytic solution can also be found easily for the case of the rectangular channel. Obviously, this inviscid solution also satisfies the non-slip condition for viscous flow on the porous surface. Dunlap et al. [3] investigated how well Culick's solution simulates actual viscous laminar flow in a circular pipe using sintered bronze (with very fine pore size) as the porous material, and found that the experimental results agree strikingly well with the prediction. To explain this agreement, the authors noted that the net viscous force acting on a small fluid element is negligible compared with the net pressure force. Several other experiments have been carried out to study the type of flow with different measurement techniques and experimental apparatus. Some details are shown in Table 1. Olson and Eckert [4] investigated the flow field in a porous pipe and found that the flow pattern without entrance, as in a rocket, was very different from that with entrance flow. Yamada et al. [5] examined the axial and normal velocity profiles and turbulence intensity profiles in an investigation of erosive burning in a 2D channel with side injection. Dunlap et al. [6] measured the turbulence properties at various downstream locations in a cylindrical chamber with relatively low injection velocity.

Author(s)	Year	Geometry	Range of Re_w	Measurement Techniques	Quantities Measured	Porous Surface	Pore size
Olson & Eckert	1966	Pipe L/D=24	250-7500	Impact Tube	U, V, T, β	Cloth Wrapping	N/A
Yagodkin	1967	Pipe L/D=30	At least 130	Hot-Wire Photograph	U, V, σ_u, σ_v	"Carbon", "metals"	N/A
Dunlap et al.	1974	Pipe L/D=8.4	300-2500	Hot-wire	U, V, σ_u, σ_v	Sintered Bronze	5-15μm
Yamada et al.	1976	2D Channel L/H=10	N/A	Hot-wire	$U, V, \sigma_u, \sigma_v, I_t$	N/A	20μm 70μm
Traineau et al.	1986	2D Channel L/H=24	7840	2D LDV	$U, V, \sigma_u, \sigma_v, \overline{u'v'}, \beta, I_t$	Sintered Copper balls	50 μm
Dunlap et al.	1990	Pipe L/D=9.5, 14.3	4500-9000	3D Hot-wire	$U, V, \sigma_u, \sigma_v, \sigma_w, \overline{u'v'}, \overline{u'w'},$	Sintered Bronze	5-15μm
Cheng & Hwang	1995	2-D Channel L/H=40	5-20	N/A	U, V, T_w, P, T_{exit}	Ceramic fiber, graphite plate	N/A
Couton et al.	1996	2-D Channel Complex Geometery	4900	2D LDA	$U, V, \sigma_u, \sigma_v, I_t$	Sintered Poral, Metallic weave	75 μm

Table 1 Previous experimental investigations of internal flows related to Solid Rocket Motors

Regarding transition, Beddini [7] predicted three regions of behavior: Region I, furthest upstream, in which the laminar theory holds; Region II, called the transition region, in which the mean velocity profiles and turbulent statistics undergo transition from the laminar case; And Region III, after the transition region, in which turbulence dominates, and the velocity profiles become steeper close to the wall. Similar transition behavior was also observed in the experiments at high injection Reynolds numbers performed by Traineau et al [8]. However, the transition points predicted by different authors vary significantly, depending on the facility and simulation.

Experimental appratus and techniques

Test channel

An apparatus to produce a canonical, non-reacting turbulent channel flow with fully transpired wall has been constructed, and is shown schematically in Figure 1. The total length of the channel L is 1,626 mm, and the channel height H is 76.2 mm, giving a length to height ratio (L/H) of 21. With 533 mm width and aspect ratio of 7, two-dimensional flow is assumed. Air is sucked into the channel through the top foam and the honeycomb by a high-pressure direct-drive blower. The top foam sheet (38 mm in thickness) creates a large pressure drop, making the pressure drop due to velocity increase in the channel negligible, and thereby ensuring nearly uniform injection along the wall.

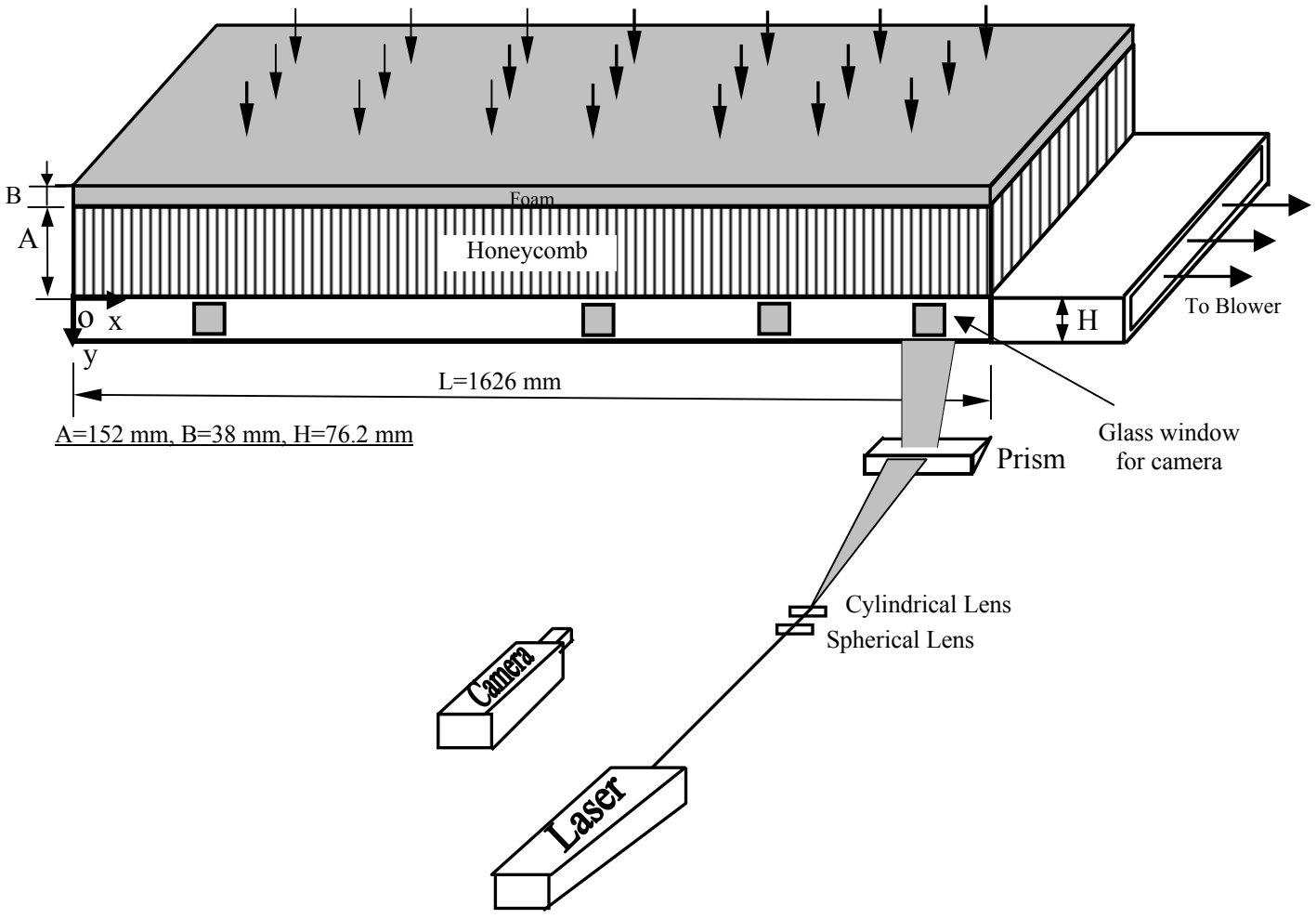

Figure 1 Schematic of experimental apparatus

Porous surfaces and flow parameters

Two types of porous surface are used: 6.35 mm honeycomb and 3.175 mm honeycomb, defined as Case I and Case II. Both honeycombs are Plascore polycarbonate honeycomb, which has uniform properties and inherently stable cells. Some dimension data and hydrodynamic impedance data are listed in Table 2 and important flow parameters are presented in Table 3. Mean values of the wall normal injection velocity V_w in Table 3 are found from two-dimensional control volume analysis by integrating through streamwise mean velocity profiles at four downstream locations. The value of V_w found at the four different locations is constant to within ±5% peak to peak.

Table 2 Dimension data and hydrodynamic impedance of the honeycombs

	Surface	Cell size	Cell pattern	Thickness A	Center spacing	Open area
Case I	6.35 mm honeycomb	3.175 mm	Staggered	152.4 mm	3.572 mm	71.7%
Case II	3.175 mm honeycomb	6.35 mm	Staggered	152.4 mm	7.144 mm	71.7%

	Zero Frequency Hydrodynamic Impedance dPw/dV_w [Pa/(m/s)]	
Case I	Impedance of Surface (6.35 mm honeycomb)	27
	Impedance of foam	1929
	Total Impedance	1956
Case II	Impedance of Surface (3.175 mm honeycomb)	124
	Impedance of foam	1942
	Total Impedance	1966

Table 3 Experimental flow parameters

	Re_w (V_wH/υ)	Injection velocity V_w (m/s)	U_{max} (m/s)			
			x/H=4	x/H=12	x/H=16	X/H=20
Case I	1531	0.307	1.31	4.02	5.16	6.80
Case II	1566	0.312	1.52	4.38	5.96	8.04

Measurement techniques

With 2D digital Particle Image Velocimetry (PIV), the instantaneous flow fields are measured in the streamwise-normal (x-y) plane at four different downstream locations with injection Reynolds numbers ($v_w H/\upsilon$) 1531 for Case I and 1566 for Case II. Optical access is obtained through a single glass window inserted into the bottom of the channel and four glass windows in the side wall. The TSI PIV system used in this paper has an acquisition rate of 15 Hz. Approximately 1000 instantaneous fields are used to calculate the mean velocity profiles and statistics for each location. Prasad et al [12] showed that the random error associated with particle displacement estimation in PIV using simple cross-correlation is approximately 5% of the particle image diameter. Therefore, in this study, since the particle images are roughly 2 pixels in diameter, the root mean square random error is about 0.1 pixels. Furthermore, since the maximum particle displacements in the PIV measurements are 10 pixels, the relative uncertainty in the PIV measurement of single instantaneous velocity vector due to error in measuring displacement is approximately 1% of the full-scale velocity. These random errors average to zero. There are also bias errors in PIV that don't average to zero. These are estimated to be less than one percent of full-scale velocity (Liu et al [14]).

Results and discussion

Laminar solution

A solution can be obtained by applying Culick's analysis [2] to the rectangular channel with one transpired wall shown in Figure 2. The solution is equivalent to solving the inviscid mean flow, Reynolds averaged Navier-Stokes equations with zero Reynolds stress. The mean velocities are given by:

$$U(x, y) = \frac{V_w \pi x}{2H} \sin(\frac{\pi y}{2H}),$$

$$V(x, y) = V_w \cos(\frac{\pi y}{2H})$$

The streamlines as predicted by above equations are plotted in Figure 2.

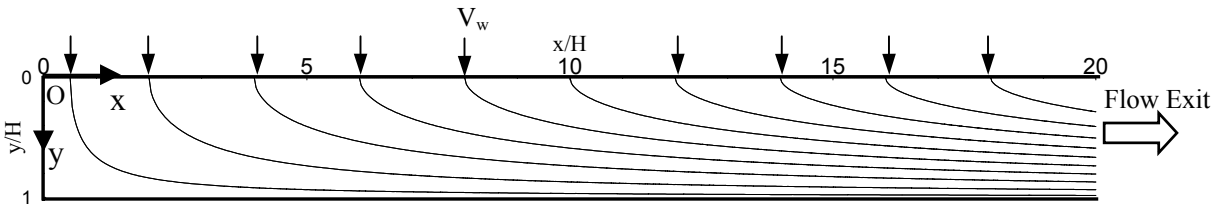

Figure 2 Streamlines of analytical solution to inviscid, zero Reynolds stress channel flow with steady, uniform one-sided injection

Instantaneous velocity fields

Two typical instantaneous velocity vector maps captured for the two different porous surfaces are shown in Figure 3. A constant velocity (area average) is subtracted from the original vector field to better reveal the differences of the two cases. For the case of 6.35 mm honeycomb (Case I), a very large turbulence level is observed. However, if the interface is replaced by a 3.175 mm honeycomb (Case II) the instantaneous velocity fields change drastically, as shown in Figure 3, and the flow pattern becomes much smoother and closer to laminar flow. Therefore, the level of turbulence varies significantly with the two different injection boundary conditions.

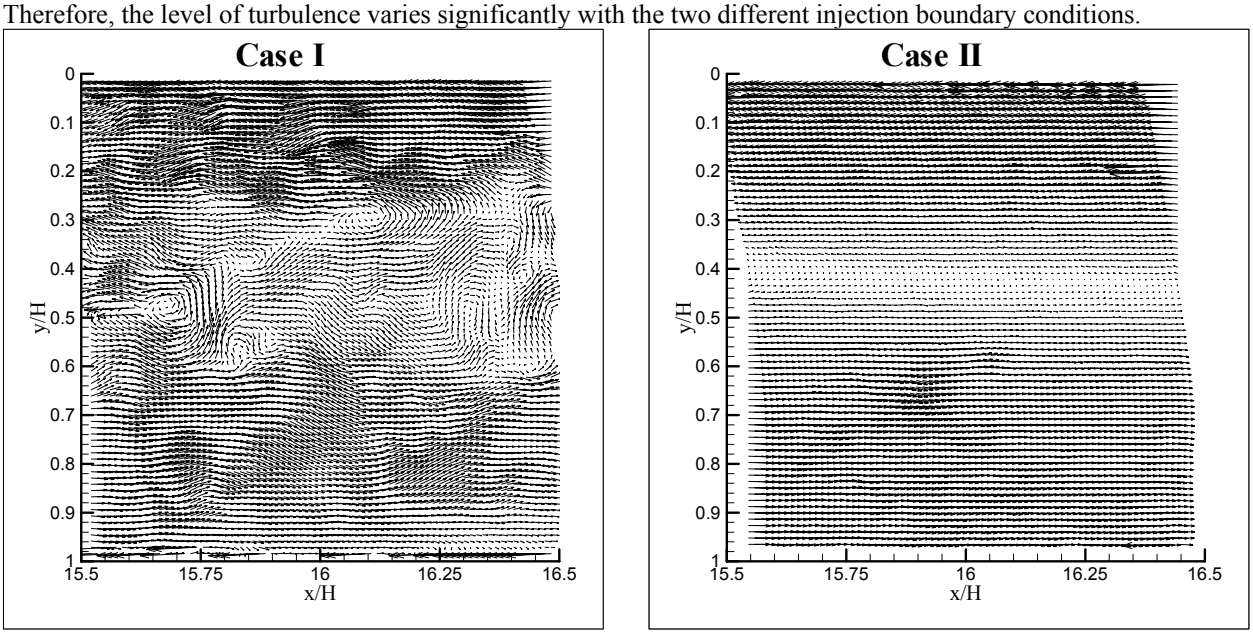

Figure 3 Instantaneous velocity vector maps for the two test cases

Mean flow properties

Figure 4 shows profiles of the mean streamwise velocity normalized by local maximum streamwise velocity at four different locations. As discussed above, there are two sets of data corresponding to the two porous surfaces used in this study. For better comparison, The analytical inviscid Reynolds stress-free solution is included and all the profiles are normalized by local maximum streamwise mean velocity. The profile of the flow created using the 3.175 mm honeycomb as the porous surface (Case II) agrees well with inviscid Reynolds stress-free solution. The flatter, more turbulent profile corresponds to the 6.35 mm honeycomb (Case I). It can be concluded that with Case II (less perturbation on the injection boundary), the mean velocity profiles agree well with the inviscid stress-free solution for a considerable downstream distance. However, if the porous surface is very coarse, and more fluctuations are created on the injection surface (Case I), the mean velocity profiles deviate significantly from the analytical stress-free solution, and look much more like the flat profiles of fully turbulent channel flow. Clearly, the details of the transpired wall boundary conditions are very important, and non-ideal wall boundary conditions can result in substantial modification in the flow structure.

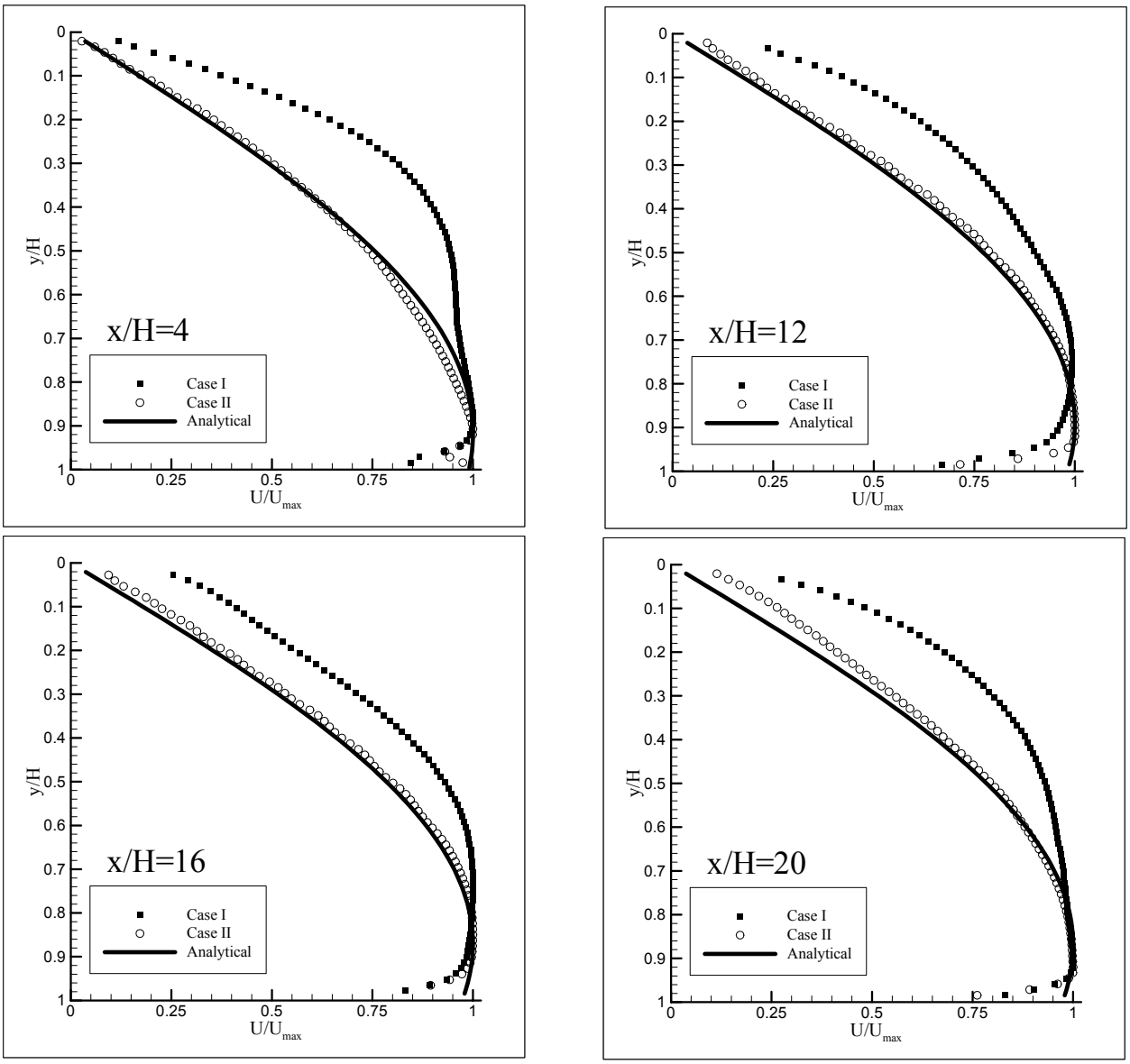

Figure 4 Mean velocity profiles at different downstream locations

Turbulence properties

Figures 5 and 6 describe respectively profiles of the RMS velocity and the Reynolds shear stress of at four locations: x/H=4, 12, 16, and 20. It is apparent that there is a peak in each profile, Also, with increasing distance downstream, the peak moves closer to the transpired surface, consistent with Beddini's computation [7]. *More importantly, Case I produces significantly higher RMS velocities and turbulence shear stresses than Case II.*

Figure 7 is obtained by averaging $\overline{v'^2}(x, y/H = 0.08)$ at different downstream locations for both cases, and choosing the maximum value of $\overline{u'v'}(x/H = 20)$ in order to relate the perturbation near the injection surface to turbulent shear stress thereafter. Both quantities are normalized by the mean injection velocity V_w. It's obvious that Case II, with higher perturbation level near the transpiration surface, causes higher turbulent shear stress than Case I with relatively lower perturbation.

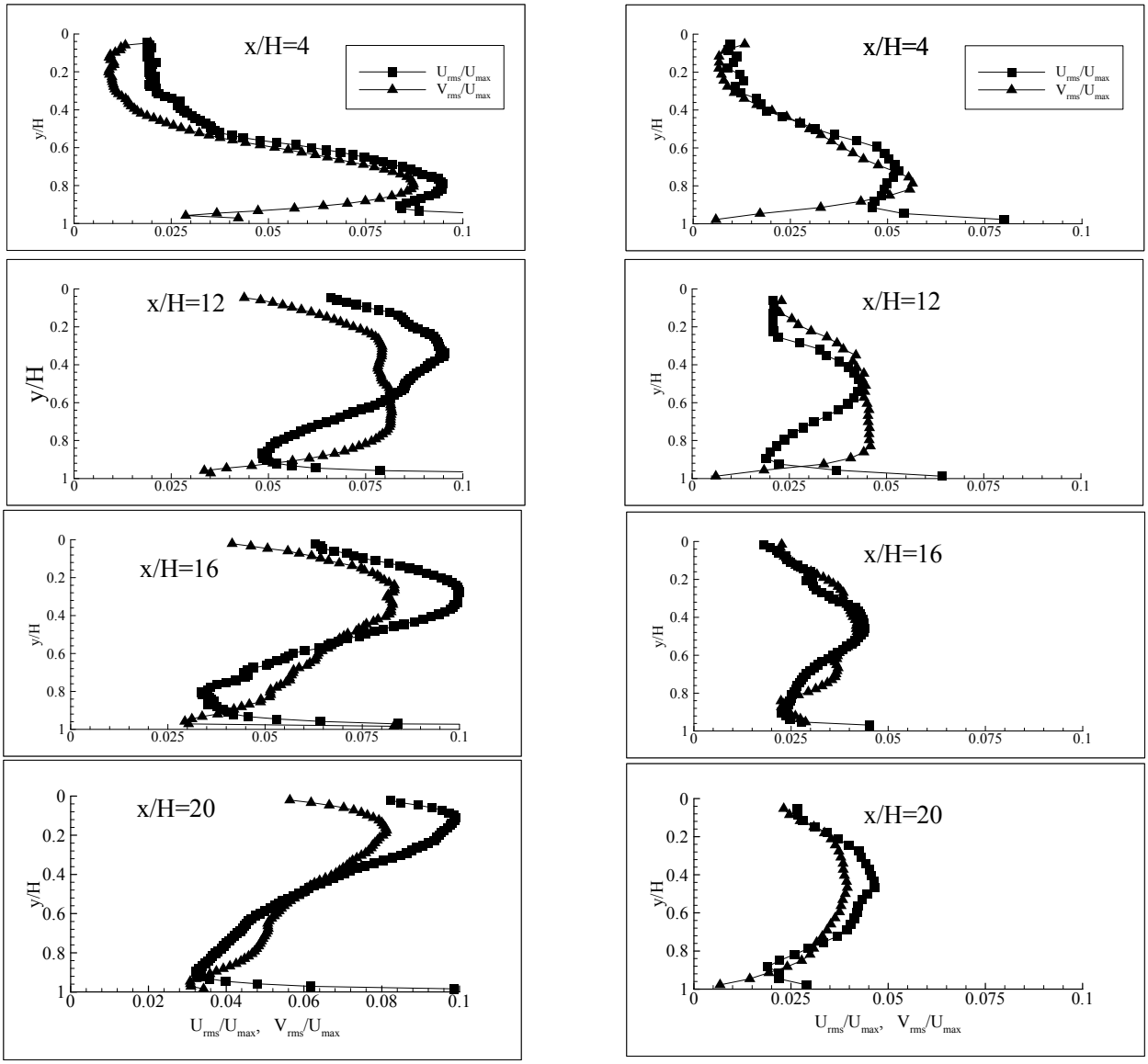

RMS velocity profiles for case I at Re_w=1531

RMS velocity profiles for case II at Re_w=1566

Figure 5 RMS velocity profiles

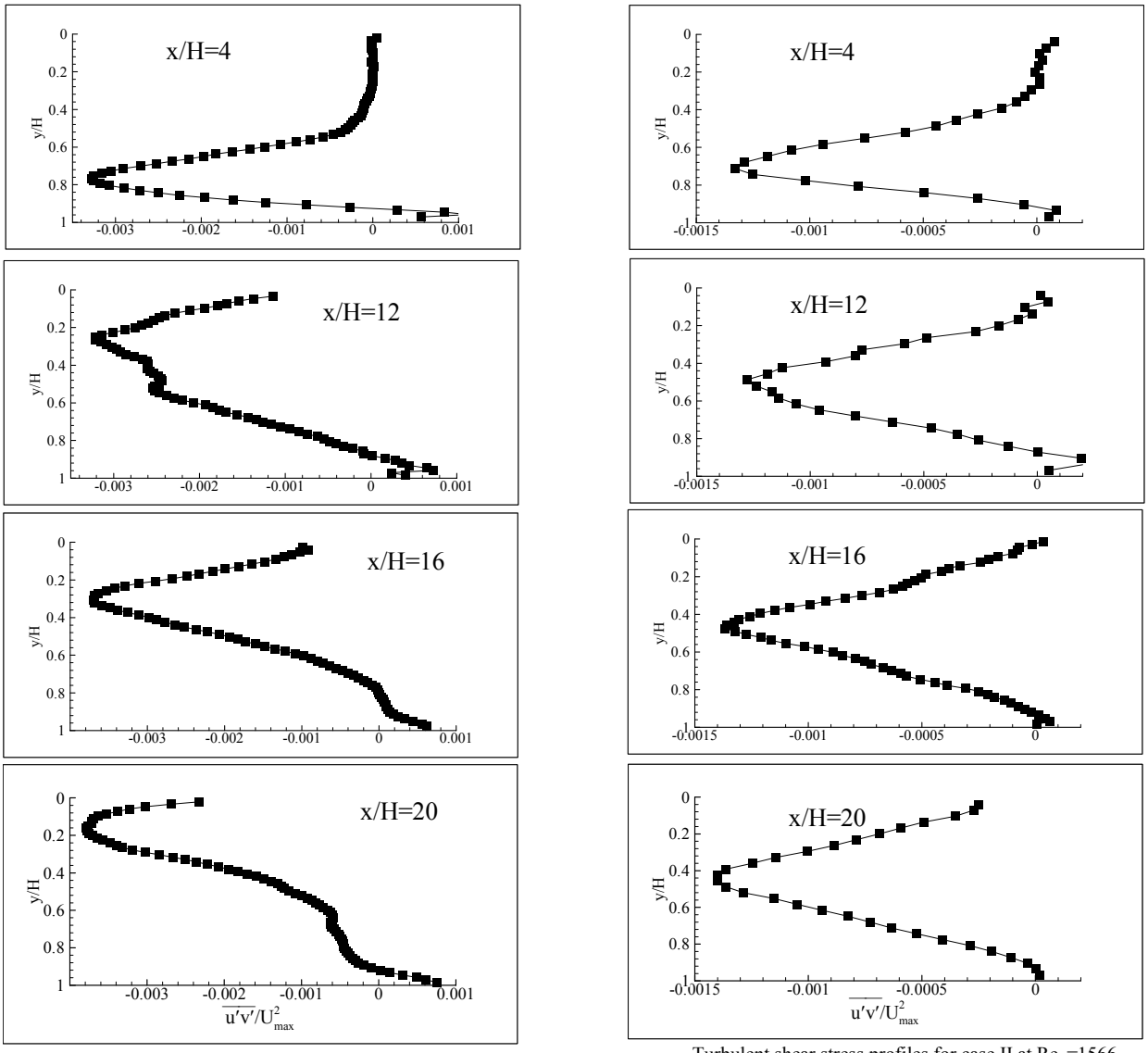

Turbulent shear stress profiles for case I at Re_w=1531

Turbulent shear stress profiles for case II at Re_w=1566

Figure 6 Turbulent shear stress profiles

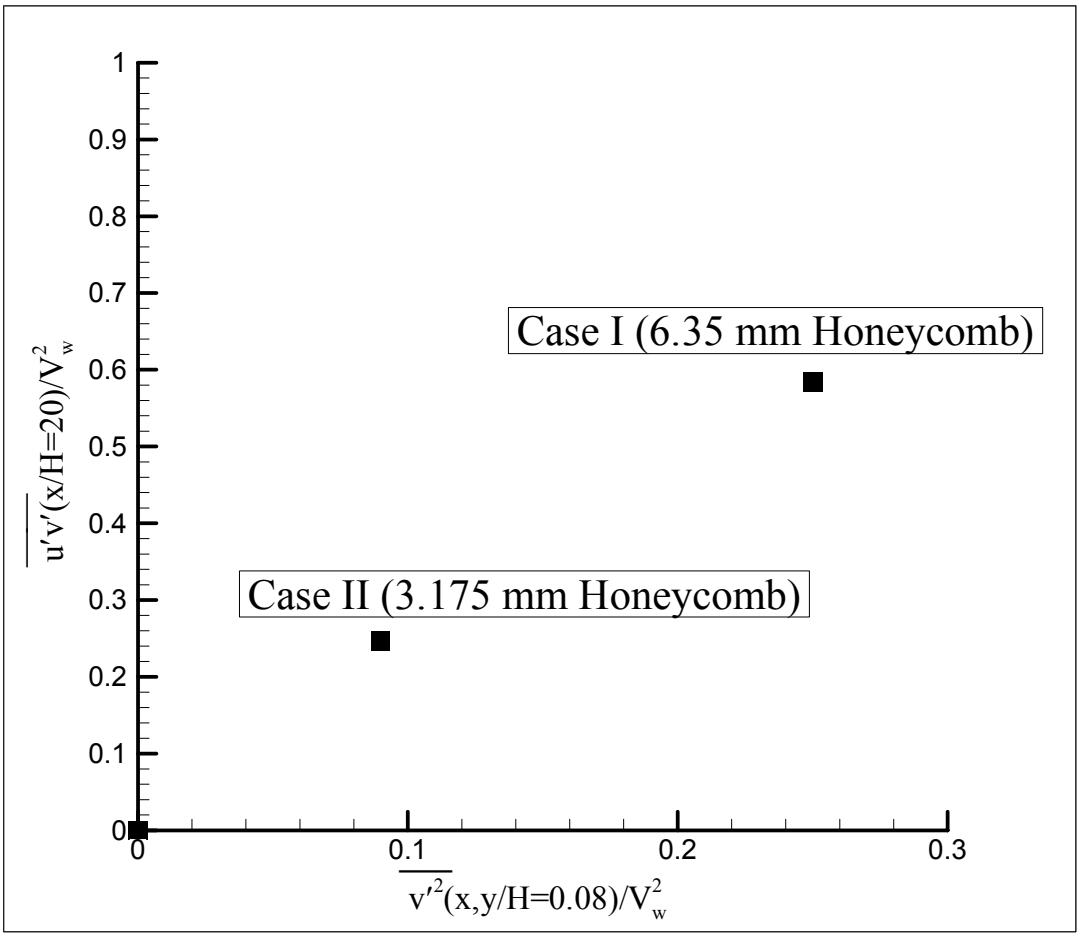

Figure 7 Relation of turbulent shear stress and perturbation near the porous surface

Summary and conclusions

Turbulence in channel flow with a fully transpired wall depends strongly upon details of the transpired wall boundary conditions. With small pore size and small perturbation on the injection surface, mean velocity profiles agree well with the analytical solution for an inviscid Reynolds stress-free flow for a considerable downstream length. This is because the turbulent Reynolds shear stress is small relatively to the mean acceleration and pressure gradient. However, if the porous surface is coarse and has higher injection fluctuations, the mean flow differs from the stress-free solution and much more turbulent shear stress is indicated. In summary, non-ideal wall boundary conditions can lead to substantial modification of the flow.

Acknowledgement

This research was supported by the Center for Simulation of Advanced Rockets (CSAR) at University of Illinois through a grant from the ASCI Program of the U.S. Department of Energy.

References

1. G. I. Taylor, 1956, Fluid Flow Regions Bounded by Porous Surfaces, Proceedings of the Royal Society of London, Series 234A, Vol. 11199, 456-475.
2. F. E. C. Culick, 1966, Rotational Axisymmetric Mean Flow and Damping of Acoustic Waves in a Solid Propellant Rocket, AIAA Journal, 1462-1464.
3. R. Dunlap, P. G. Willoughby, and R. W. Hermsen, 1974, Flowfield in the Combustion Chamber of a Solid Propellant Rocket Motor, AIAA Journal, Vol. 12, No. 10, 1440-1442.
4. R. M. Olson, and E. R. G. Eckert, 1966, Experimental Studies of Turbulent Flow in a Porous Circular Tube with Uniform Fluid Injection through the Tube Wall, Journal of Applied Mechanics, March, 7-17.
5. K. Yamada and M. Goto, 1976, Simulative Study on the Erosive Burning of Solid Rocket Motors, AIAA Journal, Vol. 14, No. 9, 1170-1176.
6. R. Dunlap, A. M. Blackner, R. C. Waugh, R. S. Brown, P. G. Willoughby, 1990, Internal Flow Field Studies in a Simulated Cylindrical Port Rocket Chamber, Journal of Propulsion, Vol. 6, No. 6, 690-704.
7. R. A. Beddini, 1985, Injection-Induced Flows in Porous-Walled Ducts, AIAA Journal, Vol. 24, No. 11, 1766-1773.
8. J. C. Traineau, P. Hervat, and P. Kuentzmann, Cold-Flow Simulation of a Two-Dimensional Nozzleless Solid-Rocket Motor, AIAA 86-1447, June 1986.
9. P. Venugopal, F. M. Najjar, and R. D. Moser, 2000, DNS and LES Computations of Model Solid Rocket Motors, AIAA 2000-3571, 36th AIAA/ASME//SAE/ASEE Joint Propulsion Conference and Exhibit, July 16-19, 2000.
10. Y. C. Cheng and G. J. Hwang, 1995, Experimental studies of laminar flow and heat transfer in a one-porous wall square duct with wall injection, Int. J. Heat Mass Transfer, Vol. 38, No. 18, 3475-3484.
11. D. Couton, F. Plourde, and S. Doan-Kim, 1996, Cold Gas Simulation of a Solid Propellant Rocket Motor, AIAA Journal, Vol. 34, No. 12, 2514-2522.
12. A. K. Prasad, R. J. Adrian, C. C Landreth, and P. W. Offutt, 1992, Effect of Resolution on the Speed and Accuracy of Particle Image Velocimetry Interrogation, Experiments in Fluids 13, 105-116.
13. R. J. Adrian, K. T. Christensen, Z.-C. Liu, 2000, Analysis and Interpretation of Instantaneous Turbulent Velocity Fields, Experiments in Fluids 29, 275-290.
14. Z. C. Liu, C. C. Landreth, R. J. Adrian, T. J. Hanrantty, 1991, High-Resolution Measurement of Turbulent Structure in a Channel with Particle Image Velocimetry. Experiments in Fluids 10, 301-312.